Conversion of Electrochemically Deposited Aragonite Crystallites to Perovskite through In Situ Ion Exchange

William D. Leal, Caroline L. Bergeron, Tyler J. Rutherford, Marek B. Majewski*

Department of Chemistry and Biochemistry and Centre for NanoScience Research, Concordia University, Montreal, QC, Canada, H4B 1R6.

ABSTRACT

The unique and broadly applicable optoelectronic properties of metal-halide perovskite materials are determined by structural dimensionality. Conversion of scaffold supported carbonate salts to perovskite with microstructure retention has previously been shown to act as a gateway to unique morphologies. In the present work, calcium carbonate microstructures are electrochemically deposited on a transparent conducting oxide substrate. Through a series of ion-exchange reactions the microstructures are decorated with a layer of surface localized perovskite nanocrystals, indicating that this ion exchange process occurs at the microstructure surface. Throughout the conversion process, electron microscopy confirms that the microstructures retain their overall morphology while cubic perovskite nanocrystals exhibiting characteristic photoluminescence and photoblinking are formed at the interface. This work confirms a synthetic pathway in which perovskites can be made in shapes previously inaccessible, which may lead to enhanced optoelectronic properties.

Introduction

Metal-halide perovskites (MHPs) are a class of crystalline materials typically adopting a cubic or orthorhombic crystal system and a chemical formula ABX_3 (A, B = cations, X = halide) where the A cation resides in a hole formed from eight corner-sharing BX_6 octahedra. They have garnered much interest in the field of solar energy conversion due to their unique optoelectronic properties, including low exciton binding energy, long charge carrier diffusion distances, and tunable band gaps.[1-3] These properties make them candidates for many light-based processes and devices, including as catalysts in chemical transformations (not limited to solar fuels generation),[4] and as active layers in photovoltaics, light-emitting diodes, and radiation detectors.[5-11] It is now well established that the optoelectronic properties of MHPs are strongly dependent on their structural and morphological dimensionality. Many of these properties are crucial to the design and implementation of solar energy conversion architectures (*e.g.*, active layers in photovoltaics) and include variations in directional transport of charge carriers, reduction of exciton recombination, and decreasing the number of trap states.[12] Recently, a wide range of MHP nanocrystal (NC) morphologies have been reported (nanowires, nanorods, nanosheets, etc.) and these typically exhibit bulk (3D) or quantum-confined (2D or 0D) properties. Developing synthetic methods to preferentially prepare specific morphologies remains an important avenue of research and coupling the properties of ensembles of the nanomaterials in microscale architectures is of additional interest (as evidenced in recent reports of MHP NC superlattices).[13]

Hybrid organic-inorganic perovskites (where the A-site cation is organic) are of great interest for their superior optoelectronic properties. Their use in photovoltaic devices has been pivotal in pushing the efficiencies of these devices to unprecedented levels, competitive with those observed in commercial crystalline silicon devices,[14] but one of their main challenges is reflected in their

poor stability (particularly with respect to heat and ambient humidity).[15-17] All-inorganic perovskites (where the A-site cation is inorganic), such as those based on cesium, lead, and halide ions, however, are expected to be more stable (presumably due to the elimination of comparatively weakly bonded organic ions) while still being a versatile and tunable material, thus making them of great interest for solar energy conversion.[15-16, 18] Many procedures exist for direct synthesis of different perovskite active layers for solar energy conversion,[8, 19-20] but often these methods limit the degree of control over the morphologies that can be prepared.[21] Target morphologies are dictated by the desired application of the material; high quality crystalline layers with fused grain boundaries for light-emitting or solar electricity applications *versus* shape and preferentially oriented, high surface area crystallites or particles for photocatalysis applications.[4]

Calcium carbonate is a material that is found with varied morphology in nature, and most typically as the thermodynamically stable calcite or aragonite and metastable vaterite polymorphs. Many of these, and modifications of their arrangements, are accessible *via* bioinspired (biomineralization) syntheses.[22] One such method is electrochemical deposition, where an applied bias initiates $CaCO_3$ deposition at a working electrode.[23] This method affords control over morphology and chirality through additives in the deposition solution, and typically results in the generation of nano- to microstructures on the electrode surface.[23] In this process, a potential is applied across an aqueous solution of sodium bicarbonate and a calcium feedstock such that electrons flow from the cathode into the solution and partially split water into H_2 and OH^- ions.[23] The resulting hydroxide ions can then deprotonate bicarbonate to yield water, leaving the resulting carbonate to react with calcium cations to produce calcium carbonate. If additives are present in the deposition solution, they may be incorporated into the crystal lattice as the deposition proceeds; as they do, they can inhibit or promote the growth of certain crystal facets, thus causing different

morphologies to form. The nature of the final structure is dependent on the identity and action of the additives themselves, where the addition of magnesium cations has previously been found to yield rosette aragonite structures while organic acids yield "barrel-like" structures.[23-24] This former behavior is based on the known relationship between the Mg/Ca ratio and temperature on calcium carbonate precipitation in sea water.[25]
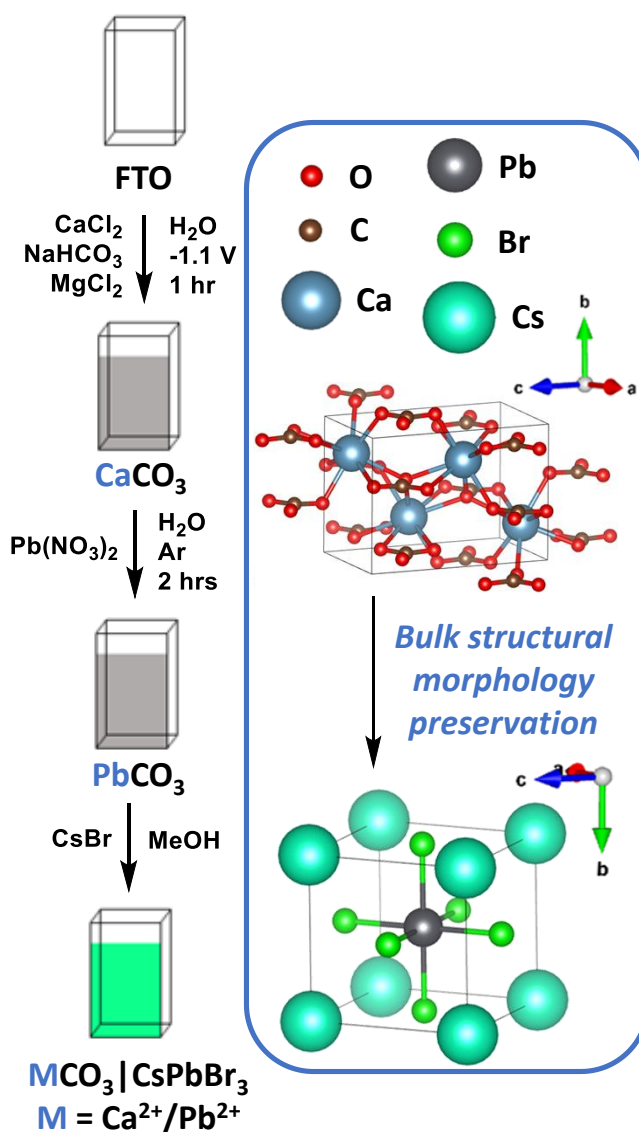
Scheme 1. Electrochemical deposition and ion-exchange conversion protocol for the calcium carbonates described in this work.

The conversion of carbonates to hybrid organic-inorganic perovskites with retention of crystal structure has been previously reported using *in situ* ion-exchange reactions to convert barium, strontium, and calcium carbonates to methylammonium lead halide perovskite on a SiO_2 scaffold.[21] The present work aims to synthesize all-inorganic cesium lead halide ($CsPbX_3$, X = Br, Cl, I) perovskite through electrochemical deposition of aragonite calcium carbonate $CaCO_3$ microstructures and subsequent conversion *via* ion-exchange (to $PbCO_3$ and finally the target MHP) with retention of hitherto inaccessible microstructure crystal morphology (Scheme 1).

Experimental Methods

Materials. Reagents for the electrochemical deposition and conversion of calcium carbonate, sodium bicarbonate ($NaHCO_3$, ACP Chemicals Inc.), calcium chloride dihydrate ($CaCl_2 \cdot 2H_2O$, Fisher), lead nitrate [$Pb(NO_3)_2$, Fisher], cesium bromide (CsBr, Alfa Aesar), magnesium chloride ($MgCl_2$, Alfa Aesar), methanol (99.8%, ACP) were used as received. The working electrode substrate used for deposition, fluorine-doped tin oxide (FTO) coated glass (Sigma-Aldrich), was cleaned through sequential three-fold sonication in soap solution (Sparkleen laboratory detergent for manual washing, Fisher), distilled water, and acetone (99.5%, Fisher) prior to use.

General Methods. All characterization methods, unless otherwise specified, were performed with the sample kept on the original FTO substrate on which it was deposited and/or converted. The microstructures on FTO were first imaged with optical microscopy using a Leitz Laborlux 11 Pol S microscope with a color Axiocam 105. Powder X-ray diffraction (PXRD) patterns were obtained using a Bruker D8 Advance (Bruker AXS, Madison, WI, USA) equipped with Cu*K*α X-ray source (wavelength, λ = 1.54 Å, radiation operating at 40 kV and 40 mA), a LYNXEYE linear position sensitive detector (Bruker AXS, Madison, WI) and a nickel filter. Data was collected using a continuous coupled θ/2θ scan in the 2θ-range of 20-60 ° with an integration time of 0.2 seconds

and step size of 0.02 °. Samples were analyzed by placing the sample slide on a zero-background silicon wafer and being manually brought to the scanning height with a raised platform. This arrangement prevented the rotation of the sample. Scanning electron microscopy (SEM) and elemental analysis by energy dispersive X-ray spectroscopy (EDS) were performed on an SEM FEG JSM-7600TFE field-emission scanning electron microscope (JEOL), with X-Max 80 SDD EDS detector (Oxford). Micrographs were obtained with an acceleration voltage of 5-10 keV, and elemental analysis was carried out with an acceleration voltage of 15 keV. Solid state emission was measured using a PTI QuantaMaster 8075 spectrofluorometer (Horiba) equipped with a 75 W Xe lamp shining through a Czerny-Turner monochromator (λ_{ex} = 350 nm) and a slide holder accessory positioned at 120 °. Samples were scanned with a step size of 1 nm and an integration time of 1 second. Diffuse reflectance spectroscopy (DRS) was performed using a Cary6000i spectrophotometer (Agilent) equipped with an integrating sphere. Fluorescence microscopy images and supporting videos were captured at 60× magnification on a Nikon Ti microscope equipped with a 60× (NA1.45) lens, and Photometrics Prime BSI camera; crystallites were illuminated with a 488 nm laser, and an appropriate filter cube (excitation: 488/10 nm, emission: 500-575 nm). Due to the high NA of the 60× lens, samples were required to be suspended in LDF Oil (R.I 1.515, 700 cSt viscosity), and covered by a #1.5 coverslip. Inductively coupled plasma mass spectrometry (ICP-MS) analysis was done using an Agilent 7500ce (Agilent). Br, Ca, Cs and Pb standards were mixed and diluted with 0.06% HCl. The calibration curves were established using the standard solutions at concentrations of 0, 0.05, 0.1, 1, and 10 ppm. Samples were run as individual batches after having been digested in 0.06% HCl. High resolution transmission electron microscopy (HR-TEM) was done using a Talos L120C TEM (Fisher) in bright field, with an accelerating voltage of 120 kV. Samples were scraped off their FTO substrate with a razor blade,

suspended in hexanes, and sonicated for 10 minutes before being deposited on 300 mesh Au TEM grids with ultrathin carbon film on lacey carbon support film (Ted Pella). Auger electron spectroscopy was performed using a JEOL JAMP-30 Auger scanning electron microscope with an accelerating voltage of 3-10 keV. Diffuse reflectance infrared Fourier transform spectroscopy (DRIFTS) spectra were collected using a Nicolet 6700 FTIR with diffuse reflectance Smart Collector accessory (Fisher).

General Deposition Procedure. The electrochemical deposition of calcium carbonate was performed by first preparing a 100 mL aqueous reaction mixture in a 100 mL volumetric flask containing 59.6 mg of $NaHCO_3$ (7.10 mM), 60.3 mg of $CaCl_2 \cdot 2H_2O$ (4.10 mM), and 61.2 mg of $MgCl_2$ (6.40 mM, for a general reaction scheme see Supporting Information Figure S1). The reaction mixture was loaded into a 100 mL beaker, and argon was bubbled through the solution for 1 hour, after which the solution was heated to 45 °C. Once this temperature was reached, bulk electrolysis was performed using a bipotentiostat (WaveDriver 20, Pine Research Instrumentation Inc.) with an applied potential of −1.1 V (vs. Ag/AgCl), with a platinum wire counter electrode and FTO working electrode, for 1 hour. Upon completion, the deposited film on FTO was rinsed with distilled water and left to air dry.

General Conversion Procedure. This conversion was performed in two separate steps. The first involved the conversion of the $CaCO_3$ to $PbCO_3$, followed by the second step where $PbCO_3$ from the first step was exposed to a solution of CsBr. The conversion of electrochemically deposited $CaCO_3$ to $PbCO_3$ was performed by first preparing an aqueous solution of $Pb(NO_3)_2$ (25 mL, 3.0 mM). This solution was transferred to a plastic 50 mL centrifuge tube and was sparged with argon for 1 hour, followed by insertion of the $CaCO_3$ FTO film under an Ar atmosphere. The FTO was left in the solution for 2 hours, after which it was removed, rinsed with distilled water, and left to

airdry. The second step of the conversion process to transform $PbCO_3$ to perovskite was carried out by first preparing a solution of CsBr (50 mL, 7.09 mM) in methanol. The $PbCO_3$ FTO was held in the solution by forceps for 30 seconds with stirring. At the end of the conversion period, the FTO was removed from the solution, rinsed with methanol, and left to air dry. The resulting FTO was kept in a desiccator (over $CaSO_4$) to preserve the quality of the perovskite material.

Results and Discussion

Electrochemical deposition of $CaCO_3$ using a modified literature procedure[23] from an aqueous solution of $NaHCO_3$ (7.10 mM), $CaCl_2 \cdot 2H_2O$ (4.10 mM), and $MgCl_2$ (6.40 mM) at 45 °C results in dendritic microstructures of $CaCO_3$ (as observed by light optical microscopy, Figure 1A). Microstructures were deposited for 1, 5, 10, 30, and 60 minutes and exhibit different morphologies between each stage of crystallite growth *via* optical microscopy (Figure S2). Powder X-ray diffraction (PXRD) patterns were recorded for each of these growth stages and it was observed that the crystallites deposited appear amorphous at low deposition times, gradually growing and more closely resembling the expected aragonite structure with prolonged deposition time (Figure S2).[26-27] Samples produced by 60 minute deposition were deemed the most suitable for further reaction as they most resembled aragonite as determined by PXRD.

Upon exposure to an aqueous $Pb(NO_3)_2$ solution, optical microscopy shows that the microstructures retain their morphology but appear less visibly transparent (Figure 1B), and, once converted in the final conversion step to $CsPbBr_3$ by exposure to a solution of CsBr in methanol, show no discernable change in appearance, once again retaining microstructure morphology (Figure 1C). Scanning electron microscopy (SEM) shows that the $CaCO_3$ microstructures are deposited with sizes on the order of 10-50 μm in length (Figure 1D). On conversion to $PbCO_3$, SEM shows that, while the microstructure morphology is maintained, the microstructures gain a

textured surface (Figure 1E). The microstructure surface initially appears as a smooth collection of fused rods or needles prior to exposure to the lead solution (Figure 1D), whereas on conversion, qualitatively, it appears as though most visible surfaces have fissured (Figure 1E). We anticipate that this change in surface texture is the result of the formation of cerussite in the interface-mediated dissolution of $CaCO_3$ and precipitation of $PbCO_3$.[28]

A recent study by Kim *et al.* provided insight into this conversion process for all three polymorphs of $CaCO_3$ and found that the mechanism is one of interface-mediated dissolution/recrystallization in acidic solution.[29-31] All three polymorphs showed the capacity to undergo the conversion, but with different efficacies dictated by solubility constant, dissolution rate, crystal habit, and surface areas of the initial microstructures. Vaterite and aragonite, growing in polycrystalline aggregates, possess higher surface area than euhedral single crystal microstructures of calcite, causing faster dissolution on exposure to an acidic solution. This leads to a faster reaction of CO_3^{2-} ions with aqueous Pb^{2+} ions, leading to preferential formation of $PbCO_3$. Vaterite was found to have a larger dissolution rate than aragonite, so that the $CaCO_3$ microstructure would dissolve more quickly than $PbCO_3$ could form, leaving a large void between the two layers. Alternatively, in aragonite, the dissolution rate and rate of $PbCO_3$ precipitation are equivalent, making it so the void at the interface between the two materials is much smaller, creating a more tightly layered composite. This causes the resulting $PbCO_3$ formed over the initial $CaCO_3$ microstructure to precipitate in much the same morphology as the layer beneath, effectively allowing for the retention of crystal morphology, though causing the change in surface texture and apparent reduction in transparency (Figures 1B, E).[29] It is anticipated that this type of cerussite shell may be porous, allowing Pb^{2+} ions in solution to migrate to the $CaCO_3/PbCO_3$ interface to continue the process of conversion to $PbCO_3$.[28, 32] The pH of the $Pb(NO_3)_2$ conversion solution in

the present work was measured and was found to be acidic with an average pH of 3.92, hence, we propose that the conversion process proceeds by the same mechanism outlined above.

Upon conversion to the anticipated final perovskite product (Figure 1F) the microstructure surface appears to be damaged while maintaining the overall microstructure morphology. This change may be brought about by the same process where the surface of the microstructure partially dissolves (on extraction of Pb^{2+}) and reacts with the ions present in solution to produce a surface layer of $CsPbBr_3$, causing a change in surface texture while retaining overall microstructure morphology.
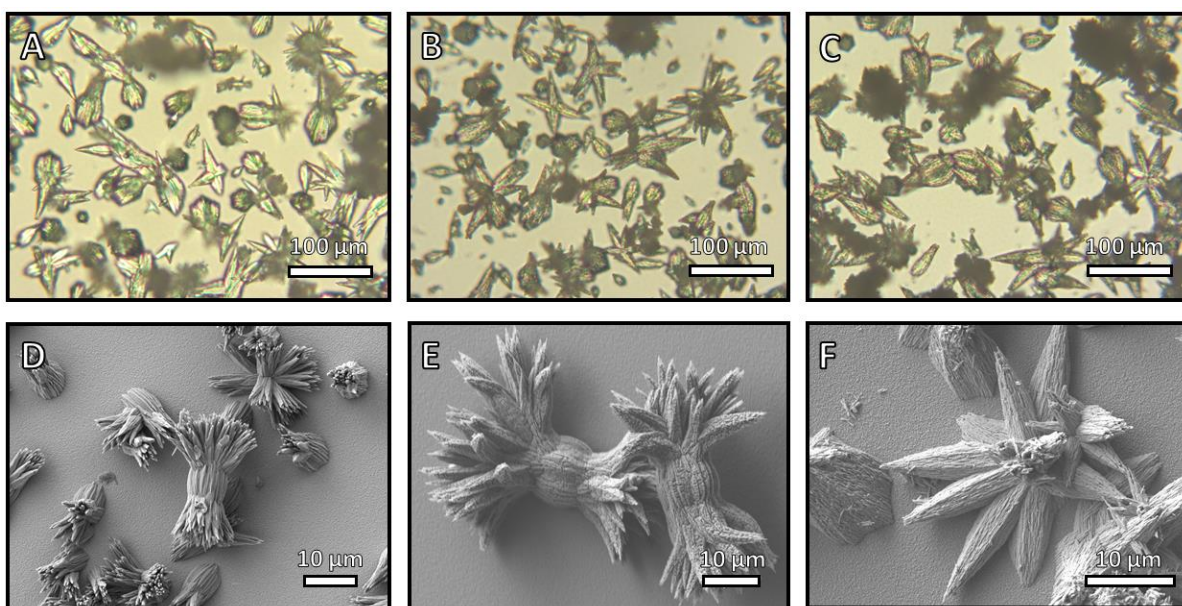
**Figure 1.** Optical micrographs of (A) $CaCO_3$ grown as aragonite, (B) microstructures after conversion to $PbCO_3$, and (C) microstructures after conversion to $CsPbBr_3$ taken at 50× magnification with (D-F) corresponding scanning electron micrographs. All samples were analyzed on the FTO substrate on which they were originally deposited and converted.

PXRD patterns were collected of the substrate fluorine-doped tin oxide (FTO) and the resultant material at each step of the deposition and conversion processes (Figure 2A). We note that the reflections at $2\theta = 26.4°$, $33.6°$, and $37.6°$ present in the collected patterns are characteristic of the

substrate FTO, as denoted by the black lines aligned with the same reflections in the pattern of the blank substrate FTO. The patterns collected for $CaCO_3$ and $PbCO_3$ resulting from electrochemical deposition and conversion, respectively, match the simulated patterns for their respective naturally occurring orthorhombic polymorphs, aragonite and cerussite. Despite repeated attempts across many samples prepared under varying conditions, the collected pattern of the final conversion product does not match the simulated pattern for cubic perovskite $CsPbBr_3$, but rather that of cerussite. This may indicate that the conversion to $CsPbBr_3$ does not permeate the entire microstructure but rather a thin surface layer.

These findings were confirmed by SEM energy dispersive X-ray spectroscopy (EDS, Figure 2B). Spectra were collected after deposition and at each conversion step, and while those of $CaCO_3$ and $PbCO_3$ adhered to expectations, $CsPbBr_3$ did not. The former showed peaks characteristic of Ca and Pb, respectively, along with C and O and atomic percentages close to the expected M:C:O ratio of 1:1:3 (M = Ca or Pb). As for the latter $CsPbBr_3$, while peaks for Pb, Cs, and Br were present, there were also peaks characteristic of C, O, and Ca. The atomic percentages collected also show Cs and Br in much lower amounts than are expected, exhibiting a Cs:Pb:Br ratio of 1:2.8:1.1 rather than the expected 1:1:3 (Table S1). However, SEM-EDS mapping data confirm the presence of Cs and Br in the general confines of the microstructure (Figure S3). Similarly, diffuse reflectance infrared Fourier transform spectroscopy (DRIFTS, Figure S4) confirms the presence of carbonates of both Pb^{2+} and Ca^{2+}. Modes at 712, 850, 1082, 1500, and 1787 cm^{-1} were observed for $CaCO_3$, and these same bands were observed in $PbCO_3$ samples along with a set of slightly shifted corresponding peaks ($\Delta \approx 42$ cm^{-1}), signifying the presence of both $CaCO_3$ and $PbCO_3$ in the $PbCO_3$ microstructures. No modes, or the disappearance of existing modes, attributable to the formation of $CsPbBr_3$ were observed.
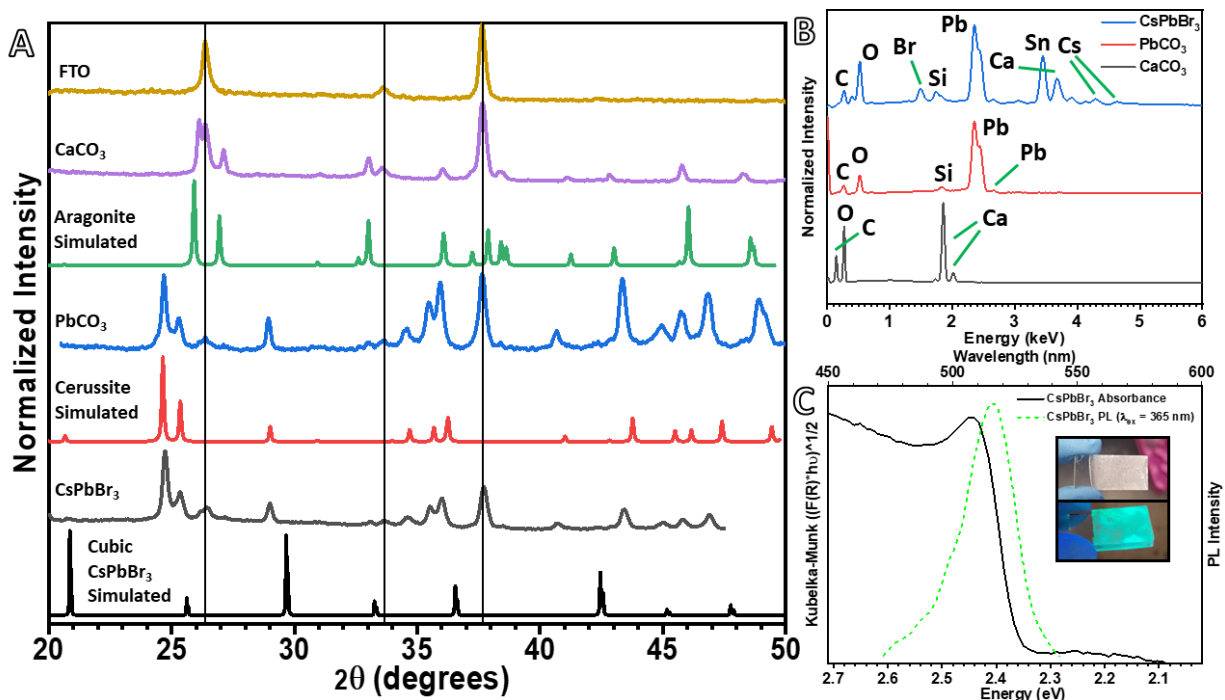
Figure 2. (A) Powder X-ray diffraction patterns of samples after deposition and ion exchange reactions with corresponding simulated patterns (CaCO$_3$ ICSD 157993, PbCO$_3$ ICSD 6178, CsPbBr$_3$ ICSD 29073). (B) Energy dispersive X-ray spectra of CaCO$_3$ after deposition, and PbCO$_3$ and CsPbBr$_3$ after respective conversion steps. (C) Diffuse Reflectance UV-Vis and photoluminescence (PL, λ_{ex} = 365 nm) spectra of CsPbBr$_3$ microstructures in the solid state on FTO slides (inset images of sample in visible and λ_{ex} = 365 nm UV light).

These techniques lack surface sensitivity, so Auger electron spectroscopy (AES) was used to analyze the chemical composition of the microstructure surface. Despite a high degree of sample degradation, peaks corresponding to Cs, Br, as well as Pb were observed along with C and O (Figure S5) correlating to our data from SEM-EDS. Analysis of SEM micrographs taken in the secondary electron scanning mode of a broken microstructure reveal a difference in chemical composition between the surface and interior of the microstructures (Figure S6). Spot SEM-EDS analysis of the surface and exposed interior show different chemical compositions where the former correlates to our earlier SEM-EDS findings, while the latter much more closely resembles CaCO$_3$ in composition (Figures 2B, S4). Taken together, these results support that each conversion

13

process does not permeate the microstructures completely, but rather up to an unspecified depth within the microstructure.

The photoluminescence (PL) of the fully converted product was measured in the solid state on the FTO substrate. An emission peak was found to be centered around 517 nm (Figure 2C), matching values reported for $CsPbBr_3$ perovskite nanocrystals (PNCs, ca. 500-520 nm, Figure S7)[33-35] rather than matching the emission maximum of $CsPbBr_3$ microstructures (ca. 530-550 nm).[36-38] The absorbance of this material was measured *via* diffuse reflectance UV-Vis spectroscopy (DRS, Figure 2C). An optical bandgap energy of 2.36 eV was determined correlating to values reported for $CsPbBr_3$ PNCs rather than microstructures.[33-38]

Fluorescence microscopy (FM) was employed to visualize the microstructures upon full conversion to determine the extent to which the microstructure surface was converted to perovskite. Figure 3A shows that photoluminescence is observed from the entire profile of the microstructures, qualitatively showing that most of the microstructure surface is converted. Different emission intensities were observed between microstructures and within the confines of individual microstructures. A video recording taken during the FM experiment scanning a small area of the sample shows that these regions of different emission intensity on individual microstructures exhibit fluorescence blinking (Supporting Video 1), a phenomenon observed previously in $CsPbBr_3$ PNCs but typically not microstructures.[35, 39-40] Fluorescence blinking is a phenomenon that is attributed to the Auger-ionization of single nanocrystals, whereby electrons are ejected from the particle and subsequent excitons relax non-radiatively to the ground state, leaving the positively charged particle non-emissive until it is neutralized.[41-43] Figure 3B is a high-contrast image showing the brightest points of fluorescence blinking on some of the sample microstructures. These points are below the resolution of the instrument (308 nm) and thus in the

nanoscale size regime. These data, taken together with the electron microscopy and PXRD data, suggest that the final conversion step results in a thin surface layer of $CsPbBr_3$ nanocrystals. This nanocrystalline layer may arise because of the dissolution of $PbCO_3$ in the surface facets and subsequent or concomitant rapid formation of $CsPbBr_3$ nanoparticles on the microstructure surface.
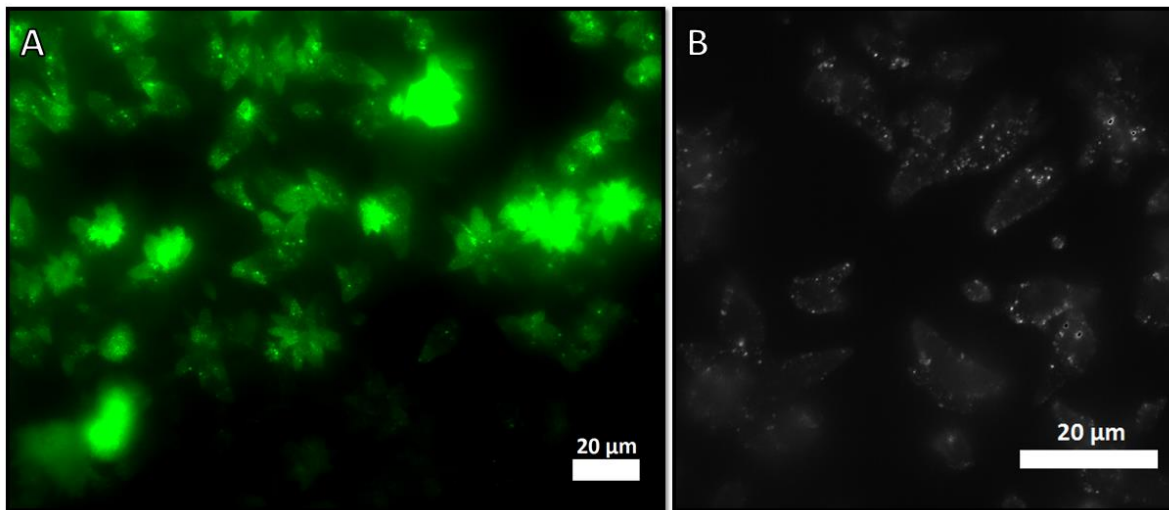

Figure 3. (A) Fluorescence microscopy image of crystallites after conversion to $CsPbBr_3$. (B) Photoblinking is observed in areas of higher contrast. (λ_{ex} = 488 nm)

We employed inductively coupled plasma mass spectrometry (ICP-MS) to better determine a chemical composition of the fully converted microstructures (Table S2). On digestion of the surface bound structure in HCl, Br and Cs were found in appreciable amounts in the samples analyzed, and a molar ratio of Cs:Br was calculated for each sample. Of the four samples analyzed (each sample being its own batch), two samples demonstrated a ratio of approximately 2.9, representing the expected stoichiometry of $CsPbBr_3$, while two samples analyzed demonstrated a ratio of approximately 5.8-6.2. This may indicate the presence of different stoichiometries, which can appear in perovskite samples due to the formation of different phases.[44-45] Furthermore, the final product in this work theoretically does not contain any organic capping groups on the

perovskite surface. In typical CsPbBr$_3$ PNC syntheses, organic surfactants are incorporated onto the nanocrystal surface to passivate it, reduce surface defects, improve colloidal/structural stability, and modulate optoelectronic properties.[46-47] In this work where as-converted material does not incorporate such a protective layer of capping groups the appearance of different stoichiometries as indicated by ICP-MS is not outside the realm of possibility.
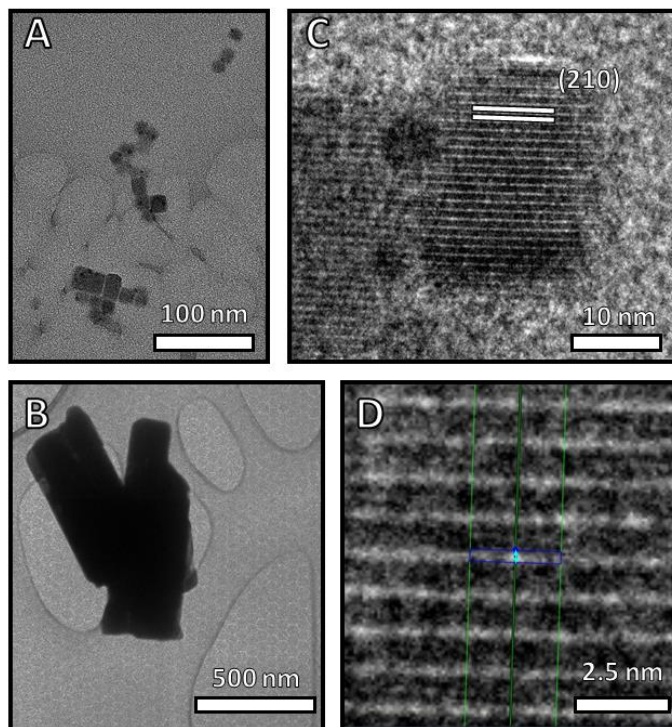
Figure 4. Transmission electron micrographs of (A) CsPbBr$_3$ nanoparticles, (B) microstructure fragments, (C) CsPbBr$_3$ nanoparticle (210) crystal plane and (D) (210) crystal plane d-spacing measurement.

Transmission electron microscopy (TEM) was used to image at an even smaller scale a sample which was scraped off the FTO surface, suspended in hexanes and sonicated (Figures 4, S8). The presence of cubic nanocrystals with an average edge length of 14.3 nm was confirmed (Figure 4A) resembling those observed from the hot-injection syntheses of CsPbBr$_3$ PNCs previously reported.[33, 39, 46] This further supports the conclusion that the surface of the final product is indeed a thin layer of CsPbBr$_3$ PNCs. Figure 4B shows a much larger set of particles, likely broken

fragments of the main body of the microstructure composed of $PbCO_3$ and $CaCO_3$. Figures 4C,D show the crystal planes of one nanocrystal found and the measurement of the interplane d-spacing (2.63 Å), which coincides with the d-spacing of the (210) crystal plane in cubic $CsPbBr_3$.

Conclusion

Electrochemically deposited aragonite $CaCO_3$ was successfully converted to the perovskite $CsPbBr_3$ with retention of overall microstructure shape, as evidenced by photoluminescence spectroscopy and fluorescence microscopy. SEM-EDS in the secondary electron scanning mode showed that exposure to a concentrated aqueous solution of $Pb(NO_3)_2$ may trigger a localized dissolution/recrystallization mechanism whereby the microstructure surface is dissolved and CO_3^{2-} reacts with Pb^{2+} in solution to form a layer of $PbCO_3$. This process is reported as being interface-mediated, causing the resulting microstructure composite to retain the morphology of the original microstructure. Transmission electron microscopy confirms that, upon exposure to CsBr in methanol, the resulting perovskite takes the form of nanoparticles on the surface of the microstructures. Fluorescence microscopy revealed that the as-converted perovskite microstructures exhibit domains of fluorescence blinking, which is a property found in $CsPbBr_3$ PNCs but not microstructures. This work confirms a synthetic pathway for producing the all-inorganic perovskite $CsPbBr_3$ in shapes previously not obtainable. Further work is ongoing to determine if properties (*e.g.*, directing of charge carriers) that might be imparted by the new morphology could prove useful in solar energy conversion and/or photocatalysis applications.

AUTHOR INFORMATION

Corresponding Author

* E-mail: marek.majewski@concordia.ca (M.B.M.)

Author Contributions

T. J. R. performed the work regarding the electrochemical deposition of $CaCO_3$ for different amounts of time. C. L. B. collected TEM micrographs and data. W. D. L. carried out all other experimental work and characterization. This manuscript was written through contributions of W. D. L. and M. B. M. All authors have given approval to the final version of the manuscript.

REFERENCES

1.   Song, J.; Xu, L.; Li, J.; Xue, J.; Dong, Y.; Li, X.; Zeng, H. Monolayer and Few-Layer All-Inorganic Perovskites as a New Family of Two-Dimensional Semiconductors for Printable Optoelectronic Devices. *Adv. Mater.* **2016,** *28* (24), 4861-4869.
2.   Akın Kara, D.; Kara, K.; Oylumluoglu, G.; Yigit, M. Z.; Can, M.; Kim, J. J.; Burnett, E. K.; Gonzalez Arellano, D. L.; Buyukcelebi, S.; Ozel, F.; Usluer, O.; Briseno, A. L.; Kus, M. Enhanced Device Efficiency and Long-Term Stability via Boronic Acid-Based Self-Assembled

Monolayer Modification of Indium Tin Oxide in a Planar Perovskite Solar Cell. *ACS Appl. Mater. Interfaces* **2018,** *10* (35), 30000-30007.

3.   Kim, Y.-H.; Cho, H.; Heo, J. H.; Kim, T.-S.; Myoung, N.; Lee, C.-L.; Im, S. H.; Lee, T.-W. Multicolored Organic/Inorganic Hybrid Perovskite Light-Emitting Diodes. *Adv. Mater.* **2015,** *27* (7), 1248-1254.

4.   Zhu, X.; Lin, Y.; San Martin, J.; Sun, Y.; Zhu, D.; Yan, Y. Lead halide perovskites for photocatalytic organic synthesis. *Nat. Commun.* **2019,** *10* (1), 2843.

5.   Zhu, H.; Fu, Y.; Meng, F.; Wu, X.; Gong, Z.; Ding, Q.; Gustafsson, M. V.; Trinh, M. T.; Jin, S.; Zhu, X. Y. Lead halide perovskite nanowire lasers with low lasing thresholds and high quality factors. *Nat. Mater.* **2015,** *14* (6), 636-642.

6.   Tan, Z.-K.; Moghaddam, R. S.; Lai, M. L.; Docampo, P.; Higler, R.; Deschler, F.; Price, M.; Sadhanala, A.; Pazos, L. M.; Credgington, D.; Hanusch, F.; Bein, T.; Snaith, H. J.; Friend, R. H. Bright light-emitting diodes based on organometal halide perovskite. *Nat. Nanotechnol.* **2014,** *9* (9), 687-692.

7.   Zhou, H.; Chen, Q.; Li, G.; Luo, S.; Song, T.-b.; Duan, H.-S.; Hong, Z.; You, J.; Liu, Y.; Yang, Y. Interface engineering of highly efficient perovskite solar cells. *Science* **2014,** *345* (6196), 542.

8.   Liu, M.; Johnston, M. B.; Snaith, H. J. Efficient planar heterojunction perovskite solar cells by vapour deposition. *Nature* **2013,** *501* (7467), 395-398.

9.   Liang, J.; Wang, C.; Wang, Y.; Xu, Z.; Lu, Z.; Ma, Y.; Zhu, H.; Hu, Y.; Xiao, C.; Yi, X.; Zhu, G.; Lv, H.; Ma, L.; Chen, T.; Tie, Z.; Jin, Z.; Liu, J. All-Inorganic Perovskite Solar Cells. *J. Am. Chem. Soc.* **2016,** *138* (49), 15829-15832.

10.   Vojvodic, A.; Nørskov, J. K. Optimizing Perovskites for the Water-Splitting Reaction. *Science* **2011,** *334* (6061), 1355.

11.   G. Kim, H.; W. Hwang, D.; Kim, J.; G. Kim, Y.; S. Lee, J. Highly donor-doped (110) layered perovskite materials as novel photocatalysts for overall water splitting. *Chem. Commun.* **1999,** (12), 1077-1078.

12.   Xu, H.; Zhang, H.; Ma, Y.; Jiang, M.; Zhang, Y.; Wu, Y.; Zhang, H.; Xia, R.; Niu, Q.; Li, X. a.; Huang, W. Morphology control of organic halide perovskites by adding BiFeO3 nanostructures for efficient solar cell. *Sci. Rep.* **2019,** *9* (1), 15441.

13.   Cherniukh, I.; Rainò, G.; Stöferle, T.; Burian, M.; Travesset, A.; Naumenko, D.; Amenitsch, H.; Erni, R.; Mahrt, R. F.; Bodnarchuk, M. I.; Kovalenko, M. V. Perovskite-type superlattices from lead halide perovskite nanocubes. *Nature* **2021,** *593* (7860), 535-542.

14.   Stoumpos, C. C.; Malliakas, C. D.; Peters, J. A.; Liu, Z.; Sebastian, M.; Im, J.; Chasapis, T. C.; Wibowo, A. C.; Chung, D. Y.; Freeman, A. J.; Wessels, B. W.; Kanatzidis, M. G. Crystal Growth of the Perovskite Semiconductor CsPbBr3: A New Material for High-Energy Radiation Detection. *Cryst. Growth Des.* **2013,** *13* (7), 2722-2727.

15.   Grancini, G.; Roldán-Carmona, C.; Zimmermann, I.; Mosconi, E.; Lee, X.; Martineau, D.; Narbey, S.; Oswald, F.; De Angelis, F.; Graetzel, M.; Nazeeruddin, M. K. One-Year stable perovskite solar cells by 2D/3D interface engineering. *Nat. Commun.* **2017,** *8*, 15684.

16.   Yang, J.; Siempelkamp, B. D.; Liu, D.; Kelly, T. L. Investigation of CH3NH3PbI3 Degradation Rates and Mechanisms in Controlled Humidity Environments Using in Situ Techniques. *ACS Nano* **2015,** *9* (2), 1955-1963.

17.   Leguy, A. M. A.; Hu, Y.; Campoy-Quiles, M.; Alonso, M. I.; Weber, O. J.; Azarhoosh, P.; van Schilfgaarde, M.; Weller, M. T.; Bein, T.; Nelson, J.; Docampo, P.; Barnes, P. R. F.

Reversible Hydration of CH3NH3PbI3 in Films, Single Crystals, and Solar Cells. *Chem. Mater.* **2015,** *27* (9), 3397-3407.

18.   Zhou, Y.; Zhao, Y. Chemical stability and instability of inorganic halide perovskites. *Energy Environ. Sci.* **2019,** *12*, 1495-1511.

19.   Lee, M. M.; Teuscher, J.; Miyasaka, T.; Murakami, T. N.; Snaith, H. J. Efficient Hybrid Solar Cells Based on Meso-Superstructured Organometal Halide Perovskites. *Science* **2012,** *338* (6107), 643.

20.   Xiao, Z.; Bi, C.; Shao, Y.; Dong, Q.; Wang, Q.; Yuan, Y.; Wang, C.; Gao, Y.; Huang, J. Efficient, high yield perovskite photovoltaic devices grown by interdiffusion of solution-processed precursor stacking layers. *Energy Environ. Sci.* **2014,** *7* (8), 2619-2623.

21.   Holtus, T.; Helmbrecht, L.; Hendrikse, H. C.; Baglai, I.; Meuret, S.; Adhyaksa, G. W. P.; Garnett, E. C.; Noorduin, W. L. Shape-preserving transformation of carbonate minerals into lead halide perovskite semiconductors based on ion exchange/insertion reactions. *Nature Chem.* **2018,** *10* (7), 740-745.

22.   Jiang, W.; Pacella, M. S.; Athanasiadou, D.; Nelea, V.; Vali, H.; Hazen, R. M.; Gray, J. J.; McKee, M. D. Chiral acidic amino acids induce chiral hierarchical structure in calcium carbonate. *Nat. Commun.* **2017,** *8* (1), 15066.

23.   Kulp, E. A.; Switzer, J. A. Electrochemical Biomineralization: The Deposition of Calcite with Chiral Morphologies. *J. Am. Chem. Soc.* **2007,** *129* (49), 15120-15121.

24.   Chen, Z.; Wang, C.; Zhou, H.; Li, X. Biomimetic Crystallization of Toplike Calcite Single Crystals with an Extensive (00.1) Face in the Presence of Sodium Hyaluronate. *Cryst. Growth Des.* **2010,** *10* (11), 4722-4727.

25.   Morse, J. W.; Arvidson, R. S.; Lüttge, A. Calcium Carbonate Formation and Dissolution. *Chem. Rev.* **2007,** *107* (2), 342-381.

26.   Walker, J. M.; Marzec, B.; Nudelman, F. Solid-State Transformation of Amorphous Calcium Carbonate to Aragonite Captured by CryoTEM. *Angew. Chem. Int. Ed.* **2017,** *56* (39), 11740-11743.

27.   Zhang, Z.; Xie, Y.; Xu, X.; Pan, H.; Tang, R. Transformation of amorphous calcium carbonate into aragonite. *J. Cryst. Growth* **2012,** *343* (1), 62-67.

28.   Yuan, K.; Lee, S. S.; De Andrade, V.; Sturchio, N. C.; Fenter, P. Replacement of Calcite (CaCO3) by Cerussite (PbCO3). *Environ. Sci. Technol.* **2016,** *50* (23), 12984-12991.

29.   Kim, Y.; Abdilla, B.; Yuan, K.; De Andrade, V.; Sturchio, N. C.; Lee, S. S.; Fenter, P. Replacement of Calcium Carbonate Polymorphs by Cerussite. *ACS Earth Space Chem.* **2021,** *5* (9), 2433-2441.

30.   Putnis, A. Mineral Replacement Reactions. *Rev. Mineral. Geochem.* **2009,** *70* (1), 87-124.

31.   Putnis, A. Mineral replacement reactions: from macroscopic observations to microscopic mechanisms. *Mineral. Mag.* **2018,** *66* (5), 689-708.

32.   Yuan, K.; Starchenko, V.; Lee, S. S.; De Andrade, V.; Gursoy, D.; Sturchio, N. C.; Fenter, P. Mapping Three-dimensional Dissolution Rates of Calcite Microcrystals: Effects of Surface Curvature and Dissolved Metal Ions. *ACS Earth Space Chem.* **2019,** *3* (5), 833-843.

33.   Protesescu, L.; Yakunin, S.; Bodnarchuk, M. I.; Krieg, F.; Caputo, R.; Hendon, C. H.; Yang, R. X.; Walsh, A.; Kovalenko, M. V. Nanocrystals of Cesium Lead Halide Perovskites (CsPbX3, X = Cl, Br, and I): Novel Optoelectronic Materials Showing Bright Emission with Wide Color Gamut. *Nano Lett.* **2015,** *15* (6), 3692-3696.

34.   Gao, Y.; Wu, Y.; Lu, H.; Chen, C.; Liu, Y.; Bai, X.; Yang, L.; Yu, W. W.; Dai, Q.; Zhang, Y. CsPbBr3 perovskite nanoparticles as additive for environmentally stable perovskite solar cells with 20.46% efficiency. *Nano Energy* **2019,** *59*, 517-526.

35.   Swarnkar, A.; Chulliyil, R.; Ravi, V. K.; Irfanullah, M.; Chowdhury, A.; Nag, A. Colloidal CsPbBr3 Perovskite Nanocrystals: Luminescence beyond Traditional Quantum Dots. *Angew. Chem. Int. Ed.* **2015,** *54* (51), 15424-15428.

36.   Lan, S.; Li, W.; Wang, S.; Li, J.; Wang, J.; Wang, H.; Luo, H.; Li, D. Vapor-Phase Growth of CsPbBr3 Microstructures for Highly Efficient Pure Green Light Emission. *Adv. Opt. Mater.* **2019,** *7* (2), 1801336.

37.   Tian, C.; Wang, F.; Wang, Y.; Yang, Z.; Chen, X.; Mei, J.; Liu, H.; Zhao, D. Chemical Vapor Deposition Method Grown All-Inorganic Perovskite Microcrystals for Self-Powered Photodetectors. *ACS Appl. Mater. Interfaces* **2019,** *11* (17), 15804-15812.

38.   Wang, Y.; Guan, X.; Li, D.; Cheng, H.-C.; Duan, X.; Lin, Z.; Duan, X. Chemical vapor deposition growth of single-crystalline cesium lead halide microplatelets and heterostructures for optoelectronic applications. *Nano Res.* **2017,** *10* (4), 1223-1233.

39.   Gibson, N. A.; Koscher, B. A.; Alivisatos, A. P.; Leone, S. R. Excitation Intensity Dependence of Photoluminescence Blinking in CsPbBr3 Perovskite Nanocrystals. *J. Phys. Chem. C* **2018,** *122* (22), 12106-12113.

40.   Behera, T.; Pathoor, N.; Phadnis, C.; Buragohain, S.; Chowdhury, A. Spatially correlated photoluminescence blinking and flickering of hybrid-halide perovskite micro-rods. *J. Lumin.* **2020,** *223*, 117202.

41.   Nirmal, M.; Dabbousi, B. O.; Bawendi, M. G.; Macklin, J. J.; Trautman, J. K.; Harris, T. D.; Brus, L. E. Fluorescence intermittency in single cadmium selenide nanocrystals. *Nature* **1996,** *383* (6603), 802-804.

42.   Li, Q.; Lian, T. Area- and Thickness-Dependent Biexciton Auger Recombination in Colloidal CdSe Nanoplatelets: Breaking the "Universal Volume Scaling Law". *Nano Lett.* **2017,** *17* (5), 3152-3158.

43.   Frantsuzov, P.; Kuno, M.; Jankó, B.; Marcus, R. A. Universal emission intermittency in quantum dots, nanorods and nanowires. *Nat. Phys.* **2008,** *4* (7), 519-522.

44.   Tong, G.; Chen, T.; Li, H.; Qiu, L.; Liu, Z.; Dang, Y.; Song, W.; Ono, L. K.; Jiang, Y.; Qi, Y. Phase transition induced recrystallization and low surface potential barrier leading to 10.91%-efficient CsPbBr3 perovskite solar cells. *Nano Energy* **2019,** *65*, 104015.

45.   Akkerman, Q. A.; Manna, L. What Defines a Halide Perovskite? *ACS Energy Lett.* **2020,** *5* (2), 604-610.

46.   Krieg, F.; Ochsenbein, S. T.; Yakunin, S.; ten Brinck, S.; Aellen, P.; Süess, A.; Clerc, B.; Guggisberg, D.; Nazarenko, O.; Shynkarenko, Y.; Kumar, S.; Shih, C.-J.; Infante, I.; Kovalenko, M. V. Colloidal CsPbX3 (X = Cl, Br, I) Nanocrystals 2.0: Zwitterionic Capping Ligands for Improved Durability and Stability. *ACS Energy Lett.* **2018,** *3* (3), 641-646.

47.   Li, J.; Xu, L.; Wang, T.; Song, J.; Chen, J.; Xue, J.; Dong, Y.; Cai, B.; Shan, Q.; Han, B.; Zeng, H. 50-Fold EQE Improvement up to 6.27% of Solution-Processed All-Inorganic Perovskite CsPbBr3 QLEDs via Surface Ligand Density Control. *Adv. Mater.* **2017,** *29* (5), 1603885.